Check for updates

# Monolayer vermiculite membranes for efficient hydrogen isotope separation†

Yihan Xu,‡[a] Xiangrui Zhang,‡[a] Tianxiang Yan,[a] Wei Liu,[a] Jianlong Lin,[a] Tianying Zhang,[a] Kai Li,[a] Xiaoyi Chen,[c] Xiao Wang,[b] Wenquan Cui [ID][b] and Sheng Zhang [ID] *[a]

H/D isotope separation faces critical challenges in terms of separation efficiency and cost. This study presents a novel, scalable fabrication of centimeter-scale, defect-free vermiculite monolayer membranes *via* a modified Langmuir–Blodgett method. These membranes demonstrate H/D separation efficiency comparable to monolayer graphene, promising cost-effective applications.

While deuterium water ($D_2O$) is commonly known for its neutron moderating properties in nuclear fission reactors, its applications extend far beyond this domain.[1] Deuterium's unique characteristics, arising from its distinct mass and nuclear spin compared to protium, make it a valuable tool in fields such as spectroscopy, chemical engineering, and pharmaceuticals.[2]

The low natural abundance of heavy water (approximately 156 ppm in nature) necessitates the development of efficient and cost-effective production methods to meet the growing demand for high-purity heavy water. Traditional industrial processes, such as the Girdler-sulfide method and 24 K cryogenic distillation, are expensive, time-consuming, and exhibit low separation factors (less than 2).[3] Consequently, recent research has focused on two primary avenues: quantum sieving and membrane-based separation. Quantum sieving techniques, utilizing the nano-confined spaces of porous materials, exploit the principles of kinetic quantum sieving (KQS) and chemical affinity quantum sieving (CAQS) to separate hydrogen isotope gas mixtures.[4–6] Materials such as porous carbon, zeolites, metal–organic frameworks, covalent organic frameworks, and

porous organic cage eutectics have shown promise in achieving efficient hydrogen isotope separation based on KQS through pore engineering. However, the remarkable $H_2/D_2$ separation ratio at extremely low temperatures (KQS: SF = 13.6 at 40 K; CAQS: SF = 11 at 100 K), hindered their industrial application. Membrane-based separation, particularly using graphene, offers an alternative approach.[7,8] Exploiting the zero-point energy (ZPE) differences and quantum tunneling effects, mechanically exfoliated monolayer graphene has achieved separation ratios of $\alpha \sim 10$ with significantly reduced energy consumption (20 GJ kg$^{-1}$).[9] This breakthrough arises from the selective permeability of monolayer graphene, allowing proton and deuteron passage while separating deuterons of lower ZPE. However, challenges remain in mitigating defects introduced during graphene growth and transfer, along with the high cost and scalability limitations of producing high-quality, large-scale monolayer graphene.[10,11] Vermiculite, an inexpensive two-dimensional material with high proton conductivity at elevated temperatures, could serve as a potential candidate for hydrogen isotope separation.[12] However, the application of atomically thin vermiculite for hydrogen isotope separation remains unexplored.

The Langmuir–Blodgett (LB) method was widely employed in fabrication of monolayer films by allowing amphiphilic molecules to self-assemble into a predictable monolayer structure at the air–liquid interface. Recent advancements have expanded the applicability of the LB method to the fabrication of large-area two-dimensional (2D) material films.[13] For instance, Li *et al.* successfully employed the LB method to create large-area monolayer graphene oxide (GO) films, which were subsequently reduced to obtain high-quality monolayer graphene.[14] Inspired by these studies, this work adapts the LB method, typically employed for graphene sheets, to fabricate large-area monolayer vermiculite films. Unlike traditional LB film fabrication, this method leverages the intrinsic physical properties of 2D flakes, rather than relying on amphiphilic behavior of monolayer, enabling the formation of a continuous vermiculite monolayer on the liquid surface (Scheme 1).

[a] *Key Laboratory for Green Chemical Technology of Ministry of Education, Collaborative Innovation Centre of Chemical Science and Engineering, School of Chemical Engineering and Technology, Tianjin University, Tianjin, P. R. China. E-mail: sheng.zhang@tju.edu.cn*

[b] *College of Chemical Engineering, Hebei Key Laboratory for Environment Photocatalytic and Electrocatalytic Materials, North China University of Science and Technology, Tangshan, China. E-mail: wqcui@ncst.edu.cn*

[c] *China Tianchen Engineering Co, Ltd, Tianjin, China*

† Electronic supplementary information (ESI) available. See DOI: https://doi.org/10.1039/d4cc04306e

‡ These authors contributed equally to this work.
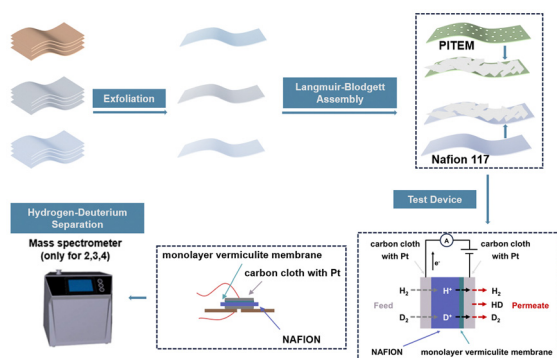
**Scheme 1** Preparation and testing process of large-scale monolayer vermiculite devices.



**Fig. 1** (a) XRD patterns of h-BN, muscovite and expanded vermiculite; (b) SEM images of expanded vermiculite, muscovite and h-BN; (c) TEM image of monolayer vermiculite, muscovite and h-BN; (d) (upper) atomic force microscope (AFM) image of monolayer vermiculite, muscovite and h-BN with silicon slice as the substrate. (lower) Height variation on white lines in AFM images. Inset: Tyndall effect of vermiculite solution, muscovite solution, and h-BN solution.

In this work, ion exchange-liquid phase exfoliation method and thermal expansion method was used to prepare monolayer dispersions of 2D materials. Then, a monolayer vermiculite membrane was prepared on PITEM with a coverage of more than 99% over a 1 cm$^2$ area using an improved Langmuir–Blodgett method. The maximum H/D separation ratio of this cm-scale vermiculite membrane approached $\sim$ 9.8, close to that of graphene. This work has opened up a new path for hydrogen isotope separation using a stable vermiculite monolayer membrane.

Stable monolayer dispersions of vermiculite and muscovite were prepared *via* ion exchange, while monolayer BN dispersions were obtained through thermal expansion. Fig. 1a presents the XRD patterns of the original hexagonal boron nitride (h-BN), muscovite, and expanded vermiculite. The XRD pattern of h-BN exhibits characteristic peaks corresponding to the hexagonal BN phase (JCPDS no. 034-0421).[15,16] Specifically, the peak at 26.6° is attributed to the (002) plane, while the broad peak near 42° corresponds to the (100) and (101) planes. Similarly, the XRD pattern of muscovite aligns with the monoclinic structure (JCPDS no. 007-0025), with the prominent peak near 9.9° attributed to the (002) plane.[17] The sharp and narrow XRD peaks observed for both h-BN and muscovite indicate high sample quality and good crystallinity. In contrast, the XRD pattern of expanded vermiculite displays characteristic peaks at 8.90°, 27.0°, and 44.72° (JCPDS no. 016-0613), alongside broad peaks between 25–30°, suggesting incomplete crystallinity.[18–20]

Fig. 1b illustrates the morphological characteristics of pristine expanded vermiculite, muscovite, and hexagonal boron nitride (h-BN). Low-magnification images (left) provide an overview of the materials' morphology, while high-magnification scanning electron microscopy (SEM) images (right) reveal their characteristic stacked layered structures. Transmission electron microscopy images (Fig. 1c) depict the monolayer vermiculite, muscovite, and h-BN (from left to right) morphologies. Notably, the vermiculite nanosheets exhibit a continuous and defect-free surface with lateral dimensions in the μm-scale. In contrast, the muscovite and h-BN nanosheets appear to be more fragmented, with sizes ranging from tens to hundreds of nanometers. Atomic force microscopy further corroborated the successful exfoliation into single or few-layer nanosheets. As depicted in Fig. 1d, the measured thicknesses of vermiculite,
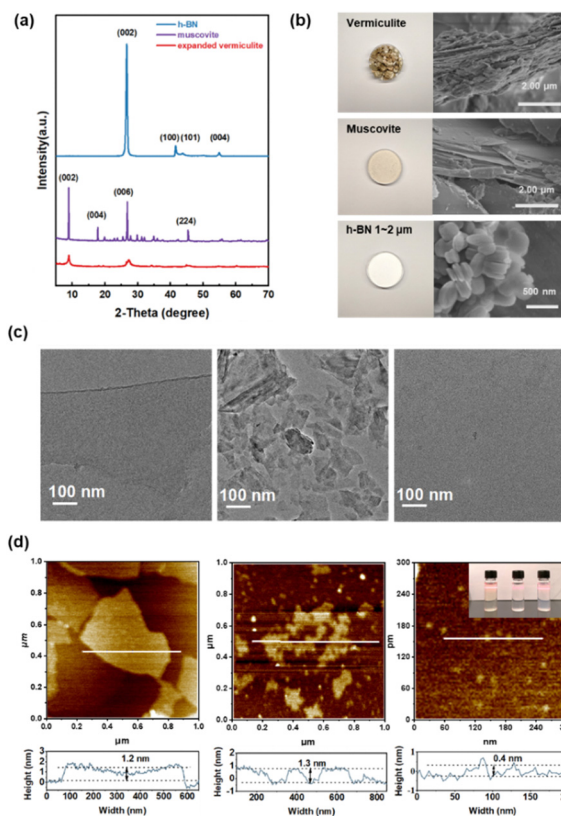
muscovite, and h-BN nanosheets were approximately 1.2 nm, 1.3 nm, and 0.4 nm, respectively. These values are consistent with the expected thicknesses of single or few-layer nanosheets, considering the $\sim$ 1 nm thickness of the underlying silicon oxide layer. Exfoliated nanosheets were dispersed in deionized water *via* cell disruption and ultrasonication, resulting in translucent yellow and milky white dispersions. As illustrated in inset of Fig. 1(d), all three nanosheet dispersions exhibit a pronounced Tyndall effect, indicating the formation of stable colloidal solutions. These dispersions remained stable for over 10 months without any visible sedimentation.[21]

A monolayer vermiculite film was prepared through a controlled interfacial assembly process, as illustrated in Fig. 2(a).[14,22–24] The influence of ethanol concentration on the surface morphology and coverage of vermiculite films prepared on porous PITEM substrates was investigated using SEM. As depicted in Fig. 2(b)–(d), the pristine PITEM substrate exhibits a relatively flat surface with uniformly distributed pores, conducive to monolayer nanosheet loading.

Statistical analysis of five-point sampled SEM images revealed an average porosity of approximately 2%. The uniform pore diameter of approximately 50 nm provides sufficient
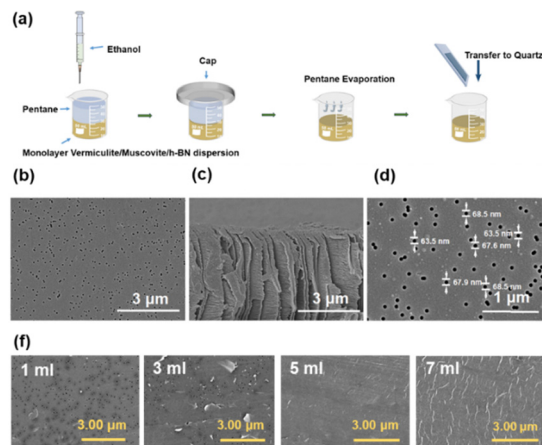
Fig. 2 (a) Schematic illustration of monolayer vermiculite, muscovite and h-BN film preparation procedure used in this work; (b) and (d) SEM image of the polyimide track etched membrane (PITEM) front; (c) SEM image of the polyimide track etched membrane (PITEM) section; (f) SEM images of monolayer vermiculite, all samples were prepared using the same method, with the variable being ethanol content. The volume fractions of ethanol are 5%, 15%, 25% and 35%, respectively.
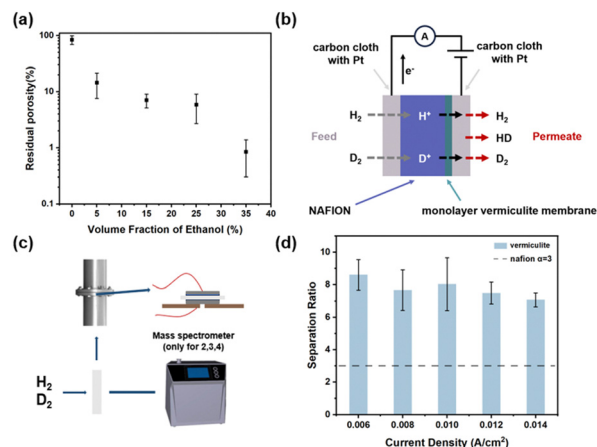


Fig. 3 (a) Porosity analysis of the monolayer vermiculite membrane; (b) schematic representation of the vermiculite device; (c) experimental setup for hydrogen isotope separation *via* mass spectrometry; (d) hydrogen–deuterium separation performance of a monolayer vermiculite membrane.

mechanical support for monolayer nanosheets, preventing cracking or collapsing, while minimizing mass transfer resistance. Increasing the volume of injected ethanol led to a corresponding decrease in the number of exposed pores on the substrate surface (Fig. 2(f)). When the volume fraction of ethanol is 25%, the vermiculite film effectively concealed the substrate pores, achieving near-complete coverage. However, exceeding this critical ethanol concentration resulted in the accelerated migration of vermiculite flakes from the bulk aqueous phase to the biphasic interface due to the poor solubility of vermiculite in ethanol. This led to flake aggregation and visible protrusions at flake edges, indicating the formation of over-stacked layers, as evidenced by the white stripes in the rightmost image of Fig. 2(f). This interfacial assembly technique was further employed to fabricate large-area monolayer films of muscovite and hexagonal boron nitride. However, SEM analysis (Fig. S1, ESI†) revealed fragmented structures for both materials on the PITEM substrate, indicating an inability to form continuous and complete films. This contrasts with monolayer vermiculite nanosheets, which, due to their larger size (diameter > 1 μm) and inherent flexibility, readily assemble into ordered films *via* the Langmuir–Blodgett (LB) method. The smaller size of monolayer muscovite and h-BN nanosheets likely hinders their orderly assembly on the PITEM substrate.

The correlation between residual porosity (ratio of exposed pores to the initial pore count) and ethanol concentration during membrane formation was investigated. As depicted in Fig. 3(a), membranes formed without ethanol exhibited a residual porosity of 83.77%. Increasing ethanol concentration to 35% led to a significant decrease of residual porosity (approximately 1%) in the large-scale monolayer vermiculite film, highlighting the efficacy of the modified L–B method. This phenomenon can be attributed to the role of ethanol as a nonsolvent to destabilize the dispersion, promoting nanosheet aggregation at the water–*n*-hexane interface.

To determine the hydrogen isotope separation rate of the fabricated vermiculite device, mass spectrometry was employed (Fig. 3c). The device, featuring a solid-state sealing design (Fig. 3b), comprises a Nafion/vermiculite membrane hot-pressed onto a Pt-loaded carbon cloth layer.[9] Electrical connections between the device electrodes and an electrochemical workstation were established using wires. For hydrogen–deuterium separation experiments, the vermiculite device was secured within a flange tube (Fig. 3c) positioned between two chambers: a feed chamber and a permeation chamber.[3] A 1 : 1 molar ratio $H_2O$–$H_2$ and $D_2O$–$D_2$ vapor–gas mixture was introduced into the feed chamber. The gas flow rate of $H_2$ and $D_2$ was maintained at 10 sccm, while the $H_2O$ and $D_2O$ vapors were supplied from cotton saturated with a 1 : 1 $H_2O$–$D_2O$ mixture within a pipe. The opposite side of the device was connected to the mass spectrometer's vacuum chamber *via* a flange tube. Upon application of a voltage, anodic oxidation of the mixed gas at the anode generated protons and deuterons. These ions permeated the Nafion/vermiculite membrane and underwent cathodic reduction at the carbon cloth, producing $H_2$, $D_2$, and HD gases.[25,26] The mass spectrometer measured the permeation flux (throughput per unit area per unit time) of the permeating gases with different relative molecular masses (2, 3, and 4). Concurrently, the electrochemical workstation monitored the current flowing through the circuit.

$$\alpha = \left(\frac{1}{2}[HD] + [H_2]\right) \Big/ \left(\frac{1}{2}[HD] + [D_2]\right)$$

The H/D separation factor ($\alpha$) was calculated according to the provided formula, where $[H_2]$, $[HD]$, and $[D_2]$ represent the changes in the flow rates of the three gases detected by the mass spectrometer before and after voltage application. As depicted in Fig. 3(d), the monolayer vermiculite device exhibited $\alpha$ values ranging from 6.7 to 9.8 across various applied current densities. This performance is approximately three times higher than that of the Nafion blank device (lacking the single-layer

vermiculite) and comparable to the reported separation factors of graphene-based devices.

At a current density of 12 mA cm$^{-2}$, the average total gas flow rate processed per square centimeter of vermiculite membrane per second was $5.77 \times 10^{-4}$ mbar L$^{-1}$. Although this demonstrates the gas handling capabilities of the membrane, industrial applications typically necessitate higher throughput. Increasing the membrane area is crucial for addressing throughput limitations. The natural abundance of vermiculite and its facile exfoliation into large-scale monolayer sheets make it a promising candidate for large-area membrane fabrication. Despite the favorable scalability of vermiculite membranes, scaling up monolayer vermiculite membrane devices for industrial hydrogen isotope separation remains a promising yet complex endeavor. Further research and development are required to optimize fabrication techniques, explore novel device architectures, and address challenges associated with large-scale implementation. By overcoming these obstacles, vermiculite membranes can become a viable and cost-effective alternative to graphene for industrial hydrogen isotope separation applications.

This study presents a novel method for fabricating large-scale, monolayer vermiculite membranes for efficient hydrogen isotope separation. This approach circumvents the limitations of traditional fabrication methods and addresses the scalability and cost barriers associated with graphene-based alternatives. The fabricated membranes exhibited remarkable hydrogen isotope separation capabilities, achieving H/D separation ratios ($\alpha$) ranging from 6.7 to 9.8, as determined by mass spectrometry. These $\alpha$ values are comparable to those reported for graphene-based devices, highlighting vermiculite's potential as a cost-effective and efficient material for this application. This work not only offers a promising alternative to graphene for large-scale hydrogen isotope separation but also paves the way for exploring the potential of other two-dimensional materials in this domain.

## Data availability

The data supporting this article have been included as part of the ESI.†

## Conflicts of interest

There are no conflicts to declare.

## Notes and references

1 J. Fu, Y. Wang, S. Das, S. Zhang, X. Zhang, H. Xiao, J. Li, T. Ben and L. Jiang, *Matter*, 2024, **7**, 2460–2472.
2 M. Glugla, R. Lässer, L. Dörr, D. Murdoch, R. Haange and H. Yoshida, *Fusion Eng. Des.*, 2003, **69**, 39–43.
3 X. Zhang, H. Wang, T. Xiao, X. Chen, W. Li, Y. Xu, J. Lin, Z. Wang, H. Peng and S. Zhang, *Langmuir*, 2023, **39**, 4975–4983.
4 N. Sun, P.-L. Li, M. Wen, J.-F. Song, Z. Zhang, W.-B. Yang, Y.-L. Zhou, D.-L. Luo and Q.-P. Zhang, *J. Mater. Sci. Technol.*, 2021, **76**, 200–206.
5 M. Liu, L. Zhang, M. A. Little, V. Kapil, M. Ceriotti, S. Yang, L. Ding, D. L. Holden, R. Balderas-Xicohténcatl, D. He, R. Clowes, S. Y. Chong, G. Schütz, L. Chen, M. Hirscher and A. I. Cooper, *Science*, 2019, **366**, 613–620.
6 F. Gao, X. Wang, W. Chen, W. Wang, W. Fan, Z. Kang, R. Wang, H. Guo, Q. Yue, D. Yuan and D. Sun, *Coord. Chem. Rev.*, 2024, **518**, 216047.
7 J. Liang, X. Zhang, T.-Q. Liu, X.-D. Gao, W.-B. Liang, W. Qi, L.-J. Qian, Z. Li and X.-M. Chen, *Adv. Mater.*, 2022, **34**, 2206524.
8 S. Yasuda, H. Matsushima, K. Harada, R. Tanii, T.-O. Terasawa, M. Yano, H. Asaoka, J. S. Gueriba, W. A. Diño and K. Fukutani, *ACS Nano*, 2022, **16**, 14362–14369.
9 M. Lozada-Hidalgo, S. Hu, O. Marshall, A. Mishchenko, A. Grigorenko, R. Dryfe, B. Radha, I. Grigorieva and A. Geim, *Science*, 2016, **351**, 68–70.
10 X. Xue, X. Chu, M. Zhang, F. Wei, C. Liang, J. Liang, J. Li, W. Cheng, K. Deng and W. Liu, *ACS Appl. Mater. Interfaces*, 2022, **14**, 32360–32368.
11 D. M. Goggin and J. R. Samaniuk, *Langmuir*, 2021, **37**, 14157–14166.
12 L. Mogg, G. P. Hao, S. Zhang, C. Bacaksiz, Y. C. Zou, S. J. Haigh, F. M. Peeters, A. K. Geim and M. Lozada-Hidalgo, *Nat. Nanotechnol.*, 2019, **14**, 962–966.
13 K. Ariga, Y. Yamauchi, T. Mori and J. P. Hill, *Adv. Mater.*, 2013, **25**, 6477–6512.
14 X. Li, G. Zhang, X. Bai, X. Sun, X. Wang, E. Wang and H. Dai, *Nat. Nanotechnol.*, 2008, **3**, 538–542.
15 B. Matović, J. Luković, M. Nikolić, B. Babić, N. Stanković, B. Jokić and B. Jelenković, *Ceram. Int.*, 2016, **42**, 16655–16658.
16 F. Khan, A. Naeem, I. U. Din, T. Saeed, M. A. Alotaibi, A. I. Alharthi, A. Habib and T. Malik, *Ceram. Int.*, 2021, **47**, 4749–4757.
17 J. Yuan, H. Ma, R. Guo, X. Ma and S. Komarneni, *ACS Sustainable Chem. Eng.*, 2020, **8**, 10920–10927.
18 B. Han, B. He, R. Geng, X. Zhao, P. Li, J. Liang and Q. Fan, *J. Mol. Liq.*, 2019, **274**, 362–369.
19 R. Wen, Z. Huang, Y. Huang, X. Zhang, X. Min, M. Fang, Y. G. Liu and X. Wu, *Energy Build.*, 2016, **116**, 677–683.
20 C. Marcos, A. Lahchich and P. Álvarez-Lloret, *Appl. Clay Sci.*, 2023, **232**, 106791.
21 M. Daab, S. Rosenfeldt, H. Kalo, M. Stöter, B. Bojer, R. Siegel, S. Förster, J. Senker and J. Breu, *Langmuir*, 2017, **33**, 4816–4822.
22 L. J. Cote, F. Kim and J. Huang, *J. Am. Chem. Soc.*, 2009, **131**, 1043–1049.
23 L. Xu, A. R. Tetreault, H. H. Khaligh, I. A. Goldthorpe, S. D. Wettig and M. A. Pope, *Langmuir*, 2019, **35**, 51–59.
24 F. Chen, S. Liu, J. Shen, L. Wei, A. Liu, M. B. Chan-Park and Y. Chen, *Langmuir*, 2011, **27**, 9174–9181.
25 M. Lozada-Hidalgo, S. Zhang, S. Hu, A. Esfandiar, I. Grigorieva and A. Geim, *Nat. Commun.*, 2017, **8**, 15215.
26 S. Bukola, Y. Liang, C. Korzeniewski, J. Harris and S. Creager, *J. Am. Chem. Soc.*, 2018, **140**, 1743–1752.